EFFECT OF INERT SPECIES ON THE STATIC AND DYNAMIC STABILITY OF A PILOTED, SWIRL-STABILIZED FLAME

Javier Rodriguez Camacho[1], Michel Akiki[2], James Blust[2], Jacqueline O'Connor[1]

[1]Pennsylvania State University, University Park, PA, USA

[2]Solar Turbines Incorporated, San Diego, CA, USA

ABSTRACT

Carbon sequestration and utilization has been proposed as a method for decarbonizing high-efficiency industrial gas turbines operating on natural gas fuels for power-generation and industrial markets. To increase the efficiency of the carbon removal process from the exhaust stream of the turbine, exhaust gas recirculation (EGR) can be used. EGR recycles a portion of the engine exhaust into the inlet, increasing the concentration of inert species in the exhaust stream to improve the performance and cost effectiveness of CO_2 separation systems. This strategy can, however, reduce the oxygen concentration in the air, leading to changes in flame stabilization in the combustor. In this study, we investigate the effect of air diluted with inert gases of different compositions and the impact that these mixtures have on flame static and dynamic stability. A swirl-stabilized flame in a single-nozzle, variable-length combustor is used to measure the flame behavior for oxygen concentrations of 15% to 21% by volume. A constant adiabatic flame temperature test matrix is conducted to mimic operation in an industrial gas turbine. High-speed chemiluminescence imaging is used to determine the change in flame shape and dynamics for each gas composition. As the oxygen concentration decreases, the flame lifts from the centerbody, resulting in an aerodynamically-stabilized flame at the lowest O_2 concentrations. Different compositions of gases result in different flame shapes, where higher levels of N_2 in the diluents result in more flame stabilization in the outer recirculation zone as compared to those with higher levels of CO_2. The flame oscillation mechanisms also change with oxygen concentration, where the lifted flames at low O_2 levels exhibit an ignition/extinction oscillation mode as compared to a vortex-shedding-coupled oscillation mode at high O_2 levels where the flame is stabilized on the centerbody. Companion chemical kinetics simulations are used to explain changes in the flame's shape and behavior.

Keywords: Combustion; Exhaust gas recirculation; Stability; Pilot flame

NOMENCLATURE

D_o	Injector outer diameter
P_{atm}	Atmospheric pressure

P'_{RMS}	Pressure fluctuation amplitude
Q'_{RMS}	Heat release rate fluctuation amplitude
S_L^o	Unstretched laminar flame speed
$S_{L,max}$	Flame speed at the extinction strain rate
T_{ad}	Adiabatic flame temperature
Π	Percentage fuel in pilot
κ_{ext}	Extinction strain rate
ϕ	Equivalence ratio

INTRODUCTION

Climate change is steadily affecting our environment, with the negative effects and risks becoming increasingly severe [1]. A major cause of climate change is greenhouse gases, carbon dioxide (CO_2) in particular. CO_2 is generated by various sectors, with power generation being a large source of CO_2 emissions. In the U.S., about 33% of CO_2 emissions came from the power sector in 2020 [2] and over 30% of the electricity generation came from the combustion of natural gas [3]. Thus, improving the emissions profile of natural gas combustion for power generation is paramount to decreasing global CO_2 emissions. Within the power-generation sector, gas turbines are one of the key technologies that rely on natural gas combustion. One strategy for reducing the climate impact of gas turbine engines is to use post-combustion CO_2 capture and sequestration (CCS).

This CCS strategy treats the combustion products using various technologies (such as absorption, distillation, and membrane separation), which can remove up to 90% of the CO_2 in the exhaust stream and store or use the CO_2 [4],[5]. A drawback to this strategy is that efficiency of capture directly depends on the concentration of CO_2 in the combustion products [4],[5],[6]. Even though CO_2 capture can be effective at low CO_2 concentrations, the process can be significantly less costly when operating with higher CO_2 levels [6]. CO_2 concentrations in combustion products from natural gas fired gas turbines range from 3% - 5% [6],[7]. One way of increasing the concentration of CO_2 is through exhaust gas recirculation (EGR). Analyses of this approach have shown that increasing the concentration of CO_2 through EGR can make the CO_2 capture process much more efficient [8],[9],[10]. The use of EGR for improved CO_2 capture is also beneficial in terms of capital cost, with standard plants requiring an investment of approximately six times that of an EGR compatible plant [8],[9].

EGR results in a semi-closed cycle that consists of returning part of the exhaust stream back into the gas turbine inlet to increase the concentration of CO_2 in the exhaust [9]. The composition of the EGR gases depends on the type of processing used on the EGR. For

example, EGR gases can be dehydrated to reduce water content or make-up oxygen can be added to improve combustion performance. The types of processing are determined by plant- and cycle-level considerations and can considerably add to the capital cost of the system. As such, the composition of EGR gases will vary from one installation to the next, sometimes by significant amounts [8].

Generally, though, recirculating the exhaust stream results in a decrease in oxygen (O_2) and an increase in nitrogen (N_2) and water content, which, alongside CO_2, act as diluents for the combustion process and alter combustion-related properties. The flame temperature can decrease depending on the diluents present in the mixture and the level of EGR used [11],[12],[13],[14]. Moreover, the addition of diluents can affect the flame speed [13],[14],[15],[16],[17] as well as the ignition delay time of a fuel/air mixture [13]. The change in mixture composition can affect other aspects of the flame, such as the structure of the flame [11]. Diluents have resulted in highly diffuse flames [12] and can even affect the underlying flow field due to the change in fluid properties [14]. These fundamental changes to combustion properties have significant implications for combustor stability, specifically the static and dynamic stability of the combustor.

The static stability of the flame is based on the flame-holding or anchoring and the range of fuel/air mixtures over which stable anchoring can be achieved. Flames can stabilize in different regions of the flow depending on the operating conditions (e.g., reactant mixture, fuel-to-air ratio, inlet temperature) [18],[19]. Changes to static stability can negatively impact engine performance. For example, studies have shown that diluents can lead to loss of flame-holding, which results in the flame being lifted from its desired anchoring point [12], [20]. The addition of diluents can result in a flame that has a wider reaction zone and extends further downstream than an air-fuel flame [12],[21]. This change in flame shape and stability could result in flames being closer to the turbine than expected. At the extreme, reductions in flame speed due to diluents in the reactant mixture could result in complete blowout of the flame [22]. These issues are important considerations for flame static stability and can be severely impacted by EGR due to changes in fluid and combustion properties.

Given the significant change in combustion properties with EGR, the dynamic stability of the flame can also be impacted, potentially leading to combustion oscillations in the combustor. Combustion oscillations are a result of heat release rate oscillations coupling with an acoustic mode in the combustor through certain intermediary mechanisms that form a closed feedback loop, resulting in self-sustained pressure and velocity oscillations inside the combustor [23]. Oscillations from dynamic instabilities can severely damage engine components and may result in degraded engine performance or even reduced engine lifetime [23]. EGR can affect the behavior of dynamic instabilities, including eliminating the dominant instability modes for certain operating conditions [24],[25]. However, this behavior depends on the EGR constituents [24].

Several strategies are used to reduce the amplitude of thermoacoustic combustion oscillations; piloting is a common strategy used in gas turbines for instability control. This strategy consists of stabilizing a flame, both statically and dynamically, by introducing a smaller secondary flame (pilot flame) in proximity to the main flame [26],[27],[28]. This flame can stabilize the combustion process by providing hot product gases at the base of the main flame [27],[29]. However, the efficacy of pilot flames for various levels of EGR has not been characterized. In particular, the pilot efficacy may change as the stabilization of the main flame changes with EGR.

The goal of this work is to investigate the changes in static and dynamic stability of a swirl-stabilized flame with the addition of varying levels of diluents. This study seeks to understand the impact of different levels of species found in EGR on flame behavior, thereby understanding the thermochemical impact of the composition of the diluents on flame stabilization and dynamics. The chosen diluent levels and compositions are based on levels and compositions expected in an industrial gas turbine engine focused on improving the CO_2 capture and sequestration process. Additionally, we test the efficacy of the pilot flame under these different diluent conditions in the hopes of extending the flame stability through the use of a central pilot.

EXPERIMENTAL OVERVIEW

Experimental Configuration

The experiment was conducted in a single-nozzle, atmospheric-pressure model combustor with a swirl-stabilized, lean-premixed main flame and a premixed central pilot flame, both running on natural gas. The combustor, shown in Figure 1, has an inlet port for the oxidizer mixture (composed of air and diluents), inlets for main fuel and pilot fuel, an acoustic forcing siren, a nozzle section, an optically accessible quartz liner, and a variable-length combustor section. The air is metered using a thermal-mass flowmeter and preheated using an 88 kW electrical heater such that the reactants are delivered at 250 °C into the combustion chamber. The diluents used in this study are CO_2, N_2, and H_2O. CO_2 and N_2 are delivered from pressurized cylinders and heat tapes are used to maintain the gases at room temperature prior to mixing with air. The H_2O used is deionized water delivered from a pressurized vessel. After metering, air and diluents are combined upstream of a choke plate to eliminate interference by the acoustic oscillations in the combustor. The water is injected as a liquid into the hot gas stream through an atomizing nozzle and is completely vaporized and well-mixed before the combustor test section.

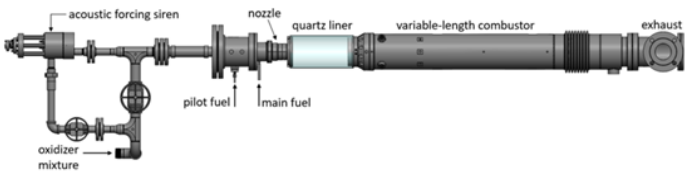

Figure 1. Experimental combustor rig showing relevant components and reactant streams.

The main fuel is injected through the leading edge of the swirler vanes in the nozzle annular passage; the nozzle velocity is held constant at 38 m/s for the entire test matrix. The pilot fuel is independently controlled from the main fuel and is injected into the centerbody. The pilot fuel mixes with a fraction of the oxidizer mixture in the centerbody and flows into the combustion chamber as an axial jet. The injector configuration is representative of industrial hardware used in modern gas turbine engines and the results from this work are applicable to a variety of injector technologies. The pilot condition used for this study is at a neutral pilot level, where 5% of fuel is delivered through the pilot centerbody. At this condition, the main flame and pilot flame equivalence ratios are approximately equal. Additionally, both the main fuel and pilot fuel are mixed with the oxidizer mixture sufficiently ahead of the dump plane such that they are technically-premixed, as described by Li et al. [26]. The nozzle outer diameter, D_o, is approximately 1.7 times the centerbody diameter and the pilot jet outlet diameter is approximately 0.3 times the centerbody diameter. The annular passage downstream of the vanes where fuel and air mix is more than two centerbody diameters in length.

The experimental rig has a quartz liner that is $2.2D_o$ in diameter and 30.5 cm long. The quartz liner allows optical access for flame imaging. Downstream of the liner is a metal variable-length section. This section allows the system to be acoustically tuned by an internal plug that can be moved using a stepper motor-controlled traverser system, resulting in a length variation of 63.5-150 cm in increments of 2.5 cm. The plug is water-cooled and the metal section around it has an inner diameter of $1.8D_o$.

Diagnostics

The rig is instrumented with K-type thermocouples to monitor the air temperature and to maintain the integrity of various components of the rig. Additionally, the rig has piezoelectric pressure transducers (PCB 113B28) that measure the dynamic pressure of the system. The transducer mounted in the dump plane measures the thermoacoustic oscillations in the combustor and there is a pair of transducers in the nozzle section used to measure the acoustic velocity of the forced fluctuations using a two-microphone method [30]. All transducers are water-cooled and recessed to prevent overheating. The transducers are operated at a sampling rate of 8192 Hz. The rig also has a digital static pressure gauge (Omega DPG1000B-05G), which is used to calculate the volumetric flow rate and the average bulk velocity in the nozzle section.

A Photron Fastcam SA4 camera coupled to an Invisible Vision UVi intensifier is used to evaluate the dynamic structure of the flame by capturing CH* chemiluminescence images. The camera is filtered using a 430±10 nm bandpass filter. Images are captured with a frame rate of 4000 frames per second and an exposure time of 250 μs. For each operating condition, eight seconds of pressure data are acquired at each combustor length and one second (4000 frames) of high-speed chemiluminescence images are taken at certain combustor lengths of interest.

Data Analysis

The pressure timeseries from the dump plane is used to study the thermoacoustic oscillations of each condition. The pressure series is evaluated in the frequency domain by using a fast Fourier transform. The oscillation frequency is selected as the maximum peak of the spectrum within a range of frequencies from 60 Hz to 600 Hz. The oscillations are characterized by determining the root-mean-squared (RMS) of the acoustic pressure fluctuation at the dump plane (P'_{RMS}) within a ± 2.5 Hz band centered about the oscillation frequency. If the pressure fluctuation is greater than 1% of atmospheric pressure (P'_{RMS}/P_{atm}), the combustor is considered unstable.

The high-speed CH* images are line-of-sight integrated images of the flame and are processed to identify the time-averaged and phase-averaged fluctuating flame structure. First, a median and an averaging filter are applied to the raw images to reduce spatial noise. The time-averaged image is the mean of the entire image set. To obtain the phase-resolved fluctuation images, the image set is filtered at the instability frequency using a fast Fourier transform on each pixel. The CH* fluctuation is used to estimate the heat release rate fluctuation and the RMS level (Q'_{RMS}) is calculated at the instability frequency. Since the flame is nominally axisymmetric, the time-average and fluctuating components are processed using an Abel inversion algorithm by applying a Hankel-Fourier operator [32]. To account for the total heat release rate associated with each pixel location, the Abel-inverted images are radially-weighted to produce images representative of CH* emission integrated over the azimuthal coordinate for each pixel of the image.

Chemical modeling

Several parameters were calculated in Chemkin-Pro [33] in order to help interpret the experimental data. The GRIMech 3.0 mechanism [31] was used to calculate adiabatic flame temperature, unstretched laminar flame speed, extinction strain rate, and flame speed at the extinction strain rate of each of the mixtures in the test matrix. The adiabatic flame temperature (T_{ad}) was held constant throughout the experiments; the equilibrium solver in Chemkin was used to determine the equivalence ratio necessary to maintain T_{ad}=1834 K for all the diluent compositions. This temperature was chosen as it is the T_{ad} for our baseline condition, where much testing had been performed in previous work [26],[27],[34]. The flame speed calculator was used to determine the unstretched laminar flame speed (S_L^o) for each mixture. The extinction strain rate (κ_{ext}) was calculated using the Opposed Flow Flame model. In this calculation, the extinction strain rate was evaluated for symmetric opposed inlets where both inlets deliver the same mixture at 523 K. For this symmetric configuration, inlet velocity is increased until complete extinction of the flame occurs, i.e. null heat release throughout the domain. The solution immediately preceding flame extinction is used to define the extinction strain rate ($\kappa_{ext,sym}$) and maximum flame

speed ($S_{L,max,sym}$). This configuration provides additional insight into the stretched flame behavior of the different mixtures tested, useful for understanding the differences in propagation and stabilization of the flame for said conditions.

RESULTS AND DISCUSSION

Test Matrix

The test matrix, outlined in Table 1, was designed based on potential EGR compositions in industrial gas turbines, with a particular focus on decreasing the O_2 mole fraction from 21% to 15%. The composition of EGR is highly dependent on the manner in which the exhaust gases are processed, including whether they are cooled, supplemented with oxygen and/or air, or dehydrated before entering the inlet of the engine. To mimic these variations, we varied O_2 concentration in two ways. One set of conditions focused on decreasing O_2 by adding higher quantities N_2 (conditions beginning with "N") and the other focused on decreasing O_2 by adding higher quantities of CO_2 (conditions beginning with "C"). Both sets include conditions with 0% and 3% H_2O. H_2O content was set to this level because the air preheater could not reliably vaporize higher flow rates of water. However, chemical modeling showed negligible sensitivity of adiabatic flame temperature and unstretched laminar flame speed to H_2O in the mixtures of interest.

To compare all compositions to the baseline condition, all conditions were tested at the same adiabatic flame temperature of 1834 K. Holding adiabatic flame temperature constant mimics the real operation of gas turbine engines, where the turbine inlet temperature is held constant as load varies. Additionally, maintaining a constant adiabatic flame temperature across the test matrix ensures that differences in the flame shape and dynamics are the result of kinetic differences in the mixture, rather than temperature differences. As the diluent level increases, an increase in equivalence ratio is required to maintain a constant adiabatic flame temperature. Although the adiabatic flame temperature is kept constant for all conditions, the flame speed decreases with increasing diluent content because of the kinetic effects of the diluents in the mixture.

Table 1. Test matrix.

Condition	O_2	CO_2	N_2	H_2O	ϕ	S_L^o [cm/s]
Baseline	0.21	0	0.79	0	0.6	44.3
C15	0.15	0.12	0.73	0	0.9	23.8
C15_H2O	0.15	0.1	0.72	0.03	0.9	24.4
C17	0.17	0.08	0.75	0	0.78	32.2
C17_H2O	0.17	0.06	0.74	0.03	0.77	32.1
C19	0.19	0.03	0.78	0	0.67	38.6

C19_H2O	0.19	0.01	0.77	0.03	0.67	39.5
N15	0.15	0.07	0.78	0	0.87	27.4
N15_H2O	0.15	0.07	0.75	0.03	0.88	26.4
N17	0.17	0.05	0.78	0	0.76	34

Time-Averaged Flame Structure

The time-averaged flame structure is highly dependent on the level of inert gas in the reactant stream. Figure 2 shows Abel-inverted images of half of the flame for each of the conditions with neutral piloting, with flow moving left to right and the centerline located at the bottom of each image. The top left image (Baseline) has a sketch of the experiment, including the location of the centerbody, pilot jet, annular jet, dump plane, centerline, and combustor wall. Two color scales are used in the images; the 17%-21% O_2 cases are on one color scale and the 15% O_2 cases are on a second color scale because the image intensity is much lower for the 15% O_2 concentration cases.

At high-O_2 conditions, the flame is stabilized on the centerbody in a V-flame configuration. The images show a gradual increase in flame length with decreasing O_2 content. This flame elongation is a result of the lower flame speed at each condition, resulting in a larger flame angle necessary to meet the kinematic condition for a constant flow velocity. Further, the addition of H_2O at each condition does not significantly impact the flame shape, which is reflected in the essentially constant flame speed between each condition and its water-addition counterpart. These images provide information about flame stabilization and flame shape but cannot provide information about the internal flame structure. Variations in the internal structure of the flame are likely given the significant variations in diluent concentration, although it is not possible to observe these changes with the current diagnostics available.

The flame shape at the 15% O_2 conditions is very different than the higher O_2 conditions. At these conditions, the flame is highly diffuse and extends far downstream; visual inspection during testing indicates that it extends into the metal section downstream of the quartz combustor. At 15% O_2 content, the flame structure is quite different for the high CO_2 and high N_2 conditions. For the high CO_2 conditions, the flame does not stabilize in the ORZ, at the top left of the images. In the high N_2 conditions, the flame stabilizes in the ORZ. Visual observation of the flame at high N_2 conditions reveals a flickering behavior in the ORZ, suggesting possible extinction and reignition.

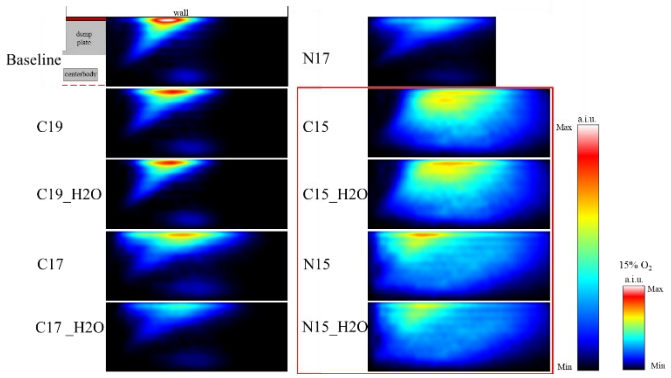

Figure 2. Time-average flame structure for various conditions under neutral piloting, centerline at the bottom of each image. Color scale for the 15% O_2 conditions (in the red box) are scaled to 1/3 of the main color scale.

The presence of the flame in the ORZ in the high N_2 conditions is likely due to the higher extinction strain rates of the flame at the high-N_2 diluent composition than the high-CO_2 compositions. The stretched flame behavior leading to extinction is illustrated in Figure 3, where the results for the opposed-flow flame model show that higher dilution leads to decreased stretched flame speeds for a given strain rate, as well as a lower extinction strain rate. In the ORZ, which is bounded by a region of high shear from the shear layer separating from the outer edge of the nozzle, the C15 mixture is likely extinguished by the higher levels of shear, whereas the N15 flame can still stabilize in this region. Similar findings have been shown in other studies of swirl-stabilized flames [18],[35],[36].

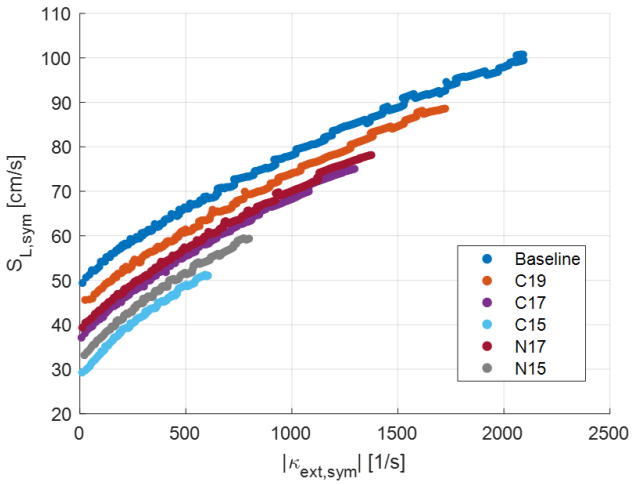

Figure 3. Stretched flame behavior calculated form a symmetric opposed flow flame model.

Instability Characteristics

The thermoacoustic oscillation amplitude and frequency are highly dependent on the composition of the reactant stream. In general, the test matrix can be separated into three different types of operating conditions that relate the static and dynamic stability characteristics. The results of the test matrix are discussed in terms of these three groupings.

The first type of conditions, Type I, are those that are well-anchored to the centerbody of the injector and display significant levels of thermoacoustic oscillation at various combustor lengths. Type I conditions include: Baseline, C19, and C19_H2O. As a result of the flame shape and anchoring position, typical velocity-coupled thermoacoustic oscillation mechanisms are present when the system is unstable (discussed in the next section). Figure 4 shows the amplitude and frequency of the instability as a function of combustor length for this first type of operating condition with neutral piloting. This behavior has been seen in previous work conducted on this experimental rig [27],[36],[37],[38].

Previous studies in this experiment have shown that three modes exist at most operating conditions: Mode I at 63.5 cm (~170 Hz), Mode III at 107 cm (~370 Hz), and Mode IV at 150 cm (~220 Hz). Mode II at 89 cm (~470 Hz) is only activated at high equivalence ratios and no dilution, which are not conditions tested in the current study. Under the Type I conditions, the combustor is unstable for two of the possible modes of this combustor. The first unstable region occurs at a combustor length of 107 cm, or Mode III. This instability oscillates at a frequency of 374 Hz and it is the strongest observed instability under neutral piloting (5% pilot). The second instability mode, Mode IV, occurs for combustor lengths of 150 cm and has an instability frequency of 226 Hz. The P'_{RMS} is higher for the 19% O_2 cases than the baseline 21% O_2 case in Mode III, but there is little difference in the instability amplitude in Mode IV. Previous studies have shown Mode III to be very sensitive to changes in operating condition, which is reflected in these results.

The second type of conditions, Type II, are those where the flame is not as strongly anchored to the centerbody but is not completely lifted: C17, C17_H2O, and N17. At these conditions, the flame is somewhat removed from the source of vortex shedding at the trailing edge of the centerbody and the combustor does not show any significant thermoacoustic oscillation over its entire length range. Figure 5 shows the amplitude and frequency of the instability as a function of combustor length for this second type of operating condition with a neutral pilot. This behavior with combustor length is similar to low equivalence ratio behavior previously seen in this combustor with no diluents [39]. In these cases, the flame speed decreases with decreasing equivalence ratio and the flame lifts from the centerbody slightly, breaking the velocity-coupled thermoacoustic feedback loop. Calculations of strained flame speed and extinction strain rate show that while the unstretched laminar flame speed at these conditions is lower than that of the Baseline case, the extinction strain rate is similar. For example, the values for the C17 case are $S_{L,max}$=75.0 cm/s and κ_{ext}=1295.6 1/s, as compared to $S_{L,max}$=100.8 cm/s and

κ_{ext}=2084.6 1/s for the Baseline. The result of these differences is a taller and more lifted flame, due to the lower flame speed, but no extinction, as a result of the high extinction strain rate.

The final type of conditions, Type III, are those where the flame is not well-anchored to the centerbody and the level of dilution is high enough that the flame is near extinction. This occurs for the following conditions: C15, C15_H2O, N15, N15_H2O. In these cases, the flame is lifted from the centerbody and highly diffuse, as seen in Figure 2. The instability has a significantly different characteristic, as seen in Figure 6, which shows that the combustor is unstable for a large, continuous range of combustor lengths, from 63.5 to 114 cm. This type of condition exhibits a low frequency of instability with a frequency that increases from 62 Hz to 80 Hz as the combustor length increases.

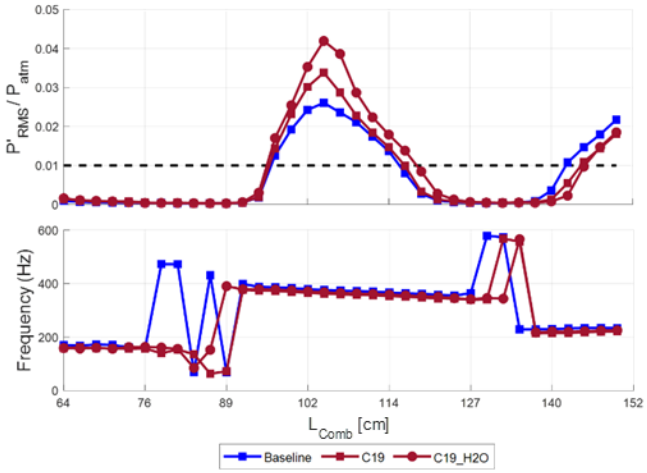

Figure 4. Stability map showing instability amplitude and frequency for Type I conditions under neutral piloting; black dashed line indicates the instability criterion.

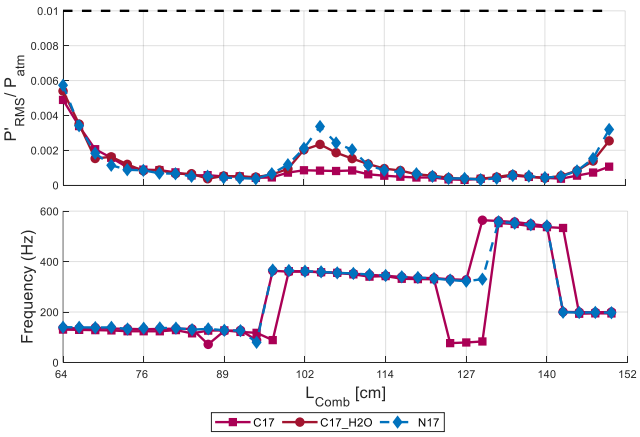

Figure 5. Stability map showing instability amplitude and frequency for Type II conditions under neutral piloting; black dashed line indicates the instability criterion.

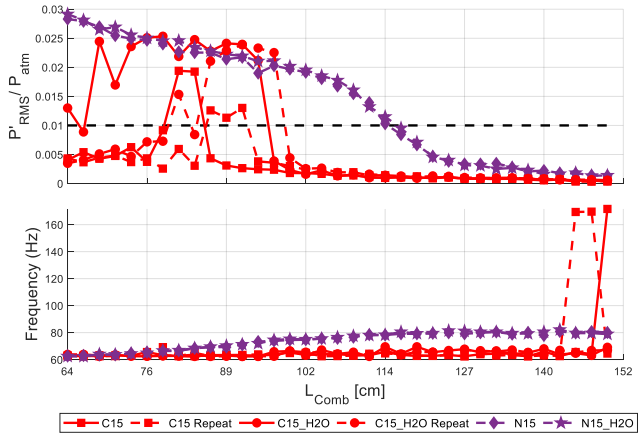

Figure 6. Stability map showing instability amplitude and frequency for Type III conditions under neutral piloting; black dashed line indicates the instability criterion.

The behavior of the Type III instability is dependent on the content of the diluents. The high N_2 conditions show a high degree of repeatability for the instability behavior and a continuous decreasing trend in amplitude as a function of combustor length. The high-CO_2 conditions are highly non-repeatable during testing and display non-monotonic behavior with increasing combustor length. The main difference between the high-N_2 and high-CO_2 conditions is the flame behavior in the ORZ. The high-N_2 conditions have a flame that is stabilized in the ORZ, though with some intermittency at shorter combustor lengths. This intermittency seems to be associated with an extinction and reignition process that may be the cause of the low-frequency instability. The lack of ORZ stabilization and more erratic instability behavior in the high-CO_2 cases is likely a result of the much lower strained flame speeds and extinction strain rates of the high-CO_2 cases. Further confirmation of the important role of the ORZ in the flame dynamical behavior is discussed with respect to flame imaging next. Finally, the frequency of the Type III cases is significantly different than that of any other thermoacoustic oscillation in the system. Further, acoustic modeling of the system does not show any mode shape with a frequency between 60 and 80 Hz in this system. The frequency is a result of the flame oscillation process and its coupling with the fluid mechanic processes in the combustor, as described next.

Unstable Flame Processes

Phase-averaged fluctuation images of the flame at these conditions are shown in Figure 7, which displays Abel-inverted images of the top half of the flame over one cycle of oscillation for various conditions. In these images, only the phase-averaged fluctuating component is shown so as to highlight the differences in oscillation pattern at different operating conditions. The color scale for each

set of images has been normalized by the maximum level at each condition; as such, the fluctuation intensities cannot be compared across images, only the fluctuation patterns.

At the baseline and 19% O_2 conditions, or Type I conditions, the flame undergoes an oscillation pattern similar to that seen in previous studies in air with velocity-coupled thermoacoustic coupling driving the oscillation [26]. A flame oscillation is excited at the base of the flame and convects along the flame front. The location of maximum flame oscillation is at the wall, where the flame oscillates upstream and downstream as the disturbance impinges on the combustor liner. The pilot flame also oscillates as a result of the thermoacoustic instability. The flame at the 17% O_2 cases, or Type II conditions, is more diffuse and very little oscillation is present as the flame is thermoacoustically stable at each combustor length. What little oscillation does occur has the same convective pattern as the Type I cases.

Oscillations at the 15% O_2 conditions are very different as compared to those with higher O_2 content. The flame is very diffuse and the oscillation does not contain a convecting pattern, but rather an extinction and re-ignition process; this observation is further confirmed

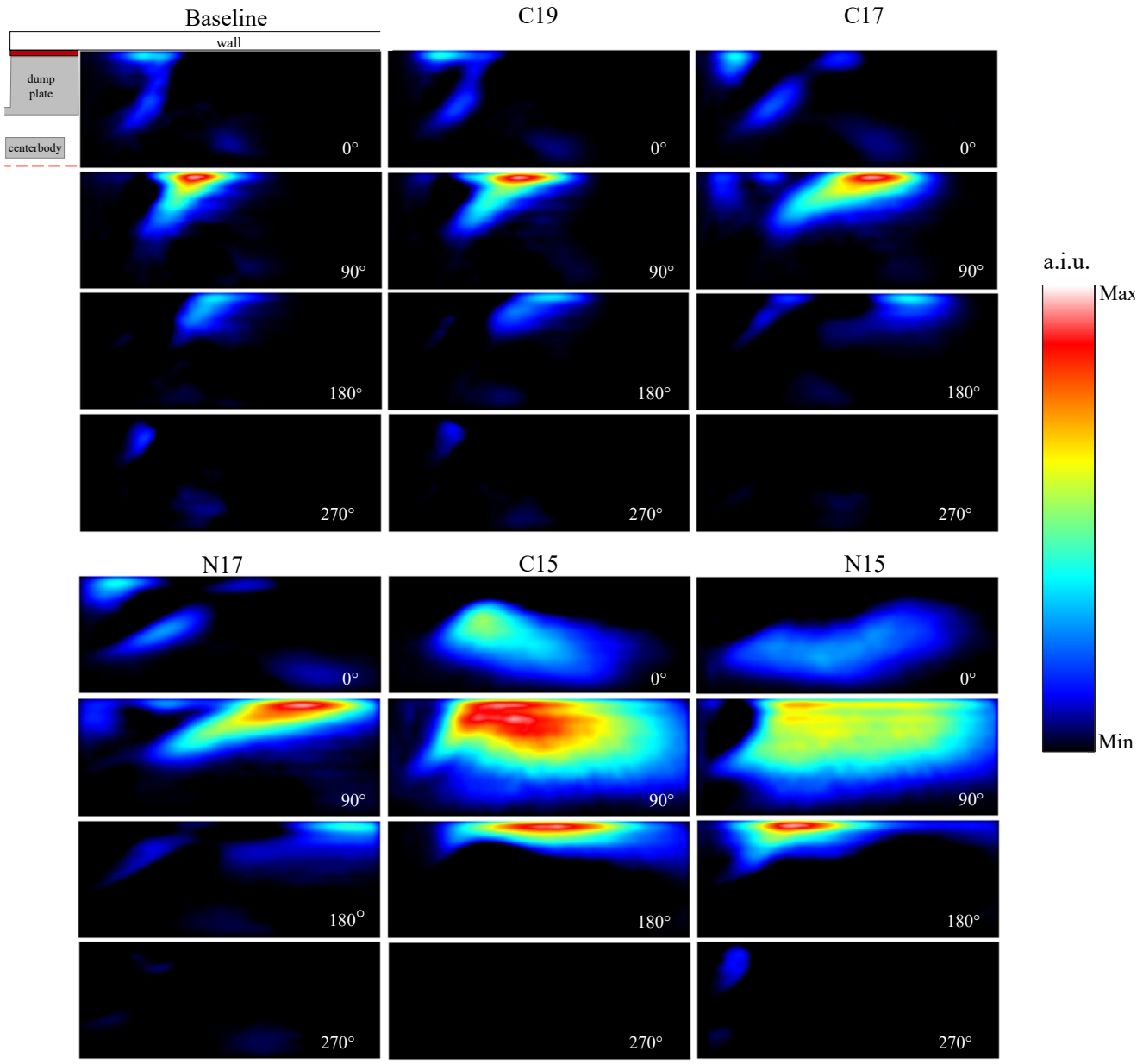

Figure 7. Top half of the phase-resolved flame oscillation over an oscillation cycle for a subset of the tested conditions with neutral piloting at a combustor length of 63.5 cm

by visual inspection of the high-speed chemiluminescence videos. The ignition process occurs near the centerline and then the flame oscillates outwards towards the combustor liner. The high-N_2 conditions show subsequent oscillations in the ORZ, whereas the high-CO_2 conditions do not, likely a result of the differences in extinction strain rate between the two mixtures. This ORZ behavior can be seen in the phase-resolved images in Figure 7 at 270° phase, where the ORZ is in the top left of each image.

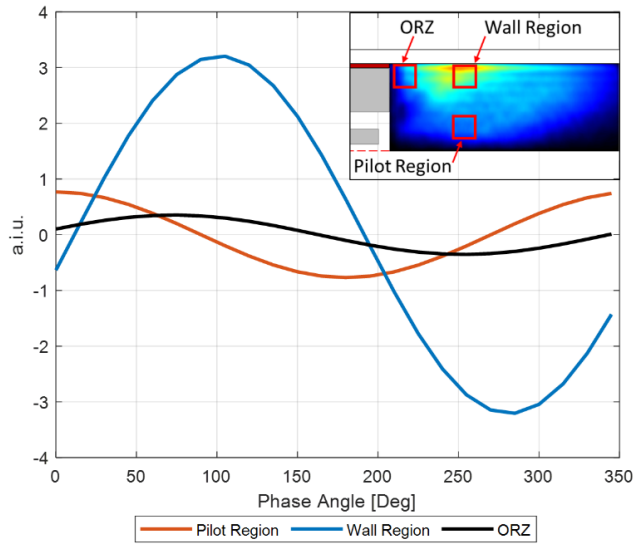

Figure 8. Progression of low-frequency instability by region for Case N15 at 63.5 cm combustor length.

The progression of the low frequency instability can be better understood by tracking the chemiluminescence fluctuation of different regions of the flame in time. To do this, we identified three regions of the flame that were dynamically significant: the pilot region, the main-flame region near the wall, and the ORZ. Signal from a 5x5 pixel interrogation window was summed in each of these regions in the phase-averaged images in order to produce a time series of chemiluminescence fluctuation. Given the phase-averaging of the images, this time series only has one frequency component at the instability frequency but can provide a better visualization of the phase between the signals to indicate which oscillation is leading versus lagging. Figure 8 shows the result of this analysis for the N15 case, with oscillation in the chemiluminescence signal for the pilot jet region, the wall region with the main flame, and the ORZ, over one oscillation cycle; the regions are shown in the inset image. At 0 degrees, the start of the cycle shows that the pilot region is close to its peak in fluctuation. The wall and ORZ regions lag behind the pilot and reach their peak fluctuation around 100 degrees after the pilot region. This phase relationship agrees with the visual observations of the high-speed imaging where the oscillation begins at the centerline, showing that the pilot region of the flame, which is located at the centerline, has an initial fluctuation that travels outward towards the wall and ORZ regions.

The low-frequency instabilities for the Type III conditions seem to be a result of ignition/extinction behaviors rather than the velocity-coupled thermoacoustic combustion instability that has been measured in this experiment previously [26],[27],[34]. To confirm this, we compare the phase-averaged results of the baseline case and the N15 case at both self-excited and open-loop forcing conditions. Open-loop forcing using a siren upstream of the combustor results in flow-rate oscillations and hence vortex shedding at the dump plane of the combustor, like the velocity-coupled instability would have. If the instability is velocity-coupled, then the phase-averaged fluctuation patterns of both the self-excited and forced-response cases should look similar. Figure 9 shows the Abel-inverted, phase-resolved flame images with self-excited on the left and open-loop forcing on the right for both conditions. In these images, only the phase-averaged fluctuating component is shown so as to highlight the oscillation pattern of the flame. In the Baseline case, the forcing frequency is set at 300 Hz, as compared to the self-excited instability frequency of 366 Hz. In the N15 case, the open-loop forcing is conducted at 80 Hz, which is the lowest frequency achievable with the current siren system and representative of the low frequencies seen in the Type III instability. Open-loop forcing was conducted at 135 cm combustor length, which was a length with no self-excited instability for any of the operating conditions.

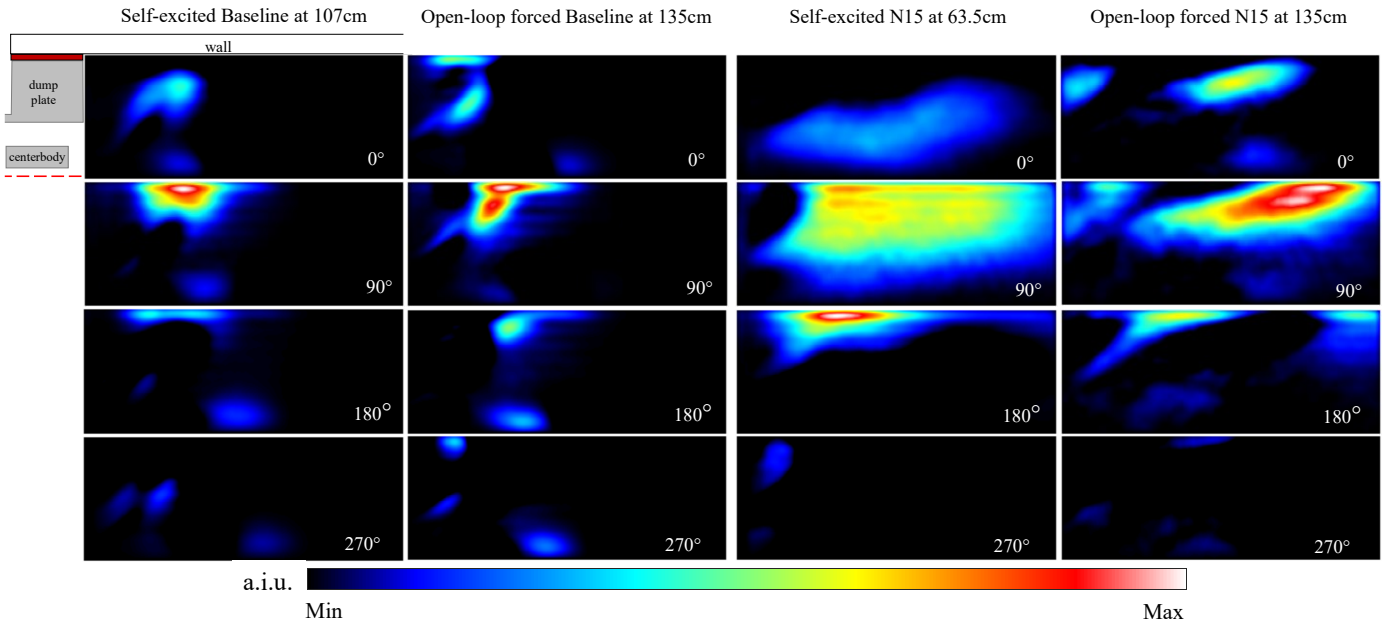

Figure 9. Top half of the phase-resolved flame oscillation over an oscillation cycle for self-excited and open-loop forced

The open-loop forcing and the self-excited behavior for the Baseline condition show similar behavior, with a flame oscillation disturbance that convects along the length of the flame. However, the self-excited and open-loop forcing conditions behave very differently in the N15 case. The open-loop forcing at 80 Hz for the N15 condition shows a breathing of the of the highly diffuse flame, which varies in length over the acoustic cycle. This behavior is consistent with very low-frequency axial velocity oscillations. However,

the self-excited case, also at a frequency of roughly 80 Hz, shows no convection or axial oscillation, indicating that the flame oscillation mechanism is not the same as would be excited by a longitudinal acoustic wave. Instead, the oscillation is the result of an extinction and re-ignition loop, where the ignition begins at the pilot flame and then an ignition wave propagates towards the wall as the fuel/air mixture that flowed into this space during the extinction period finally ignites. In the high-N_2 cases, the mixture in the ORZ also ignites, whereas this does not occur in the high-CO_2 cases. The frequency of the extinction/ignition loop is between 60 and 80 Hz, which roughly aligns with the recirculation timescales of the central recirculation zone. To estimate the recirculation timescale, time-averaged velocity data from the large-eddy simulations in Li et al. [27] were processed to determine the timescale of recirculation in this combustor at a similar flow rate. The timescale was on the same order of magnitude as the period of the oscillation, although the operating conditions in Li et al. were significantly different than the present low-O_2 conditions. As such, further investigation is necessary to confirm the hypothesis that the ignition/extinction behavior is driven by fluid-mechanic recirculation.

Based on the image analysis and velocity-field data from previous studies, the following mechanism for the oscillation in the Type III cases is proposed. The main fuel-air mixture ignites along the centerline as it meets with the pilot mixture in the central recirculation zone. This region has a longer residence time and contains hot product gases, which likely spur the ignition. The ignition wave propagates out towards the wall, consuming reactant mixture in the region of the main flame. In cases with high enough extinction strain rates (high-N_2 mixtures), the ignition can also propagate into the ORZ. However, the rapid consumption and resultant expansion of gases during the ignition wave exceeds the extinction strain rate for long enough to extinguish the flame, causing the cycle to repeat. Further flow field diagnostics could be used to confirm this hypothesis, though were out of the scope of work for the present study.

Impact of Piloting on Flame Stability

A central pilot jet was used with varying amounts of pilot fuel, while keeping the global equivalence ratio constant, to attempt to stabilize the flame both statically and dynamically. Figure 10 through Figure 12 show the impact of piloting on three conditions: Type I (Baseline), Type II (C17), and Type III (N15), respectively. In these tests, the percentage of fuel diverted to the pilot, Π, is set and then a combustor length sweep is conducted. The flow rate of air through the pilot is held constant such that the Π=0% condition has air flowing through the pilot circuit, but no fuel. At this condition, Π=5% is the neutral pilot, where the equivalence ratio of the main and pilot flames is the same. In cases where Π<5%, the pilot flame is leaner than the main flame and in cases where Π>5%, the pilot is richer than the main flame.

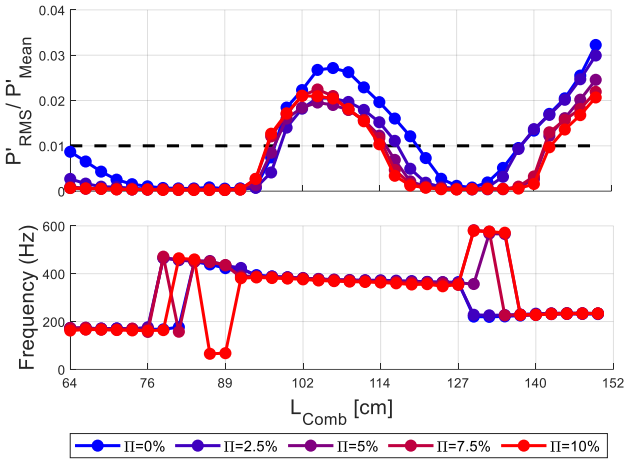

Figure 10. Stability map the Baseline (Type I) for various levels of piloting as a function of combustor length.

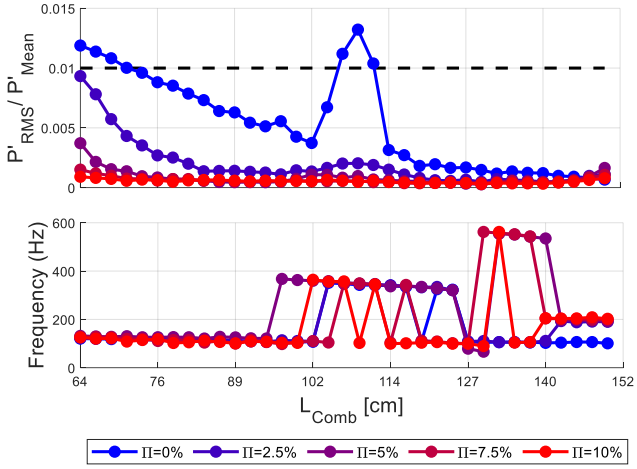

Figure 11. Stability map of C17 (Type II) for various levels of piloting as a function of combustor length.

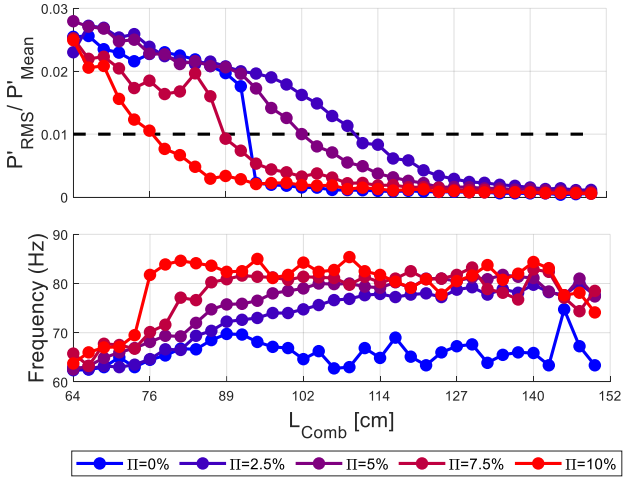

Figure 12. Stability map of N15 (Type III) for various levels of piloting as a function of combustor length.

For Type I conditions, increasing Π can reduce the instability amplitude, but not completely stabilize the combustor. Figure 10 shows the impact of piloting on the Baseline condition. The highest instability amplitude is present at Π=0% in Modes I (63.5 cm), III (107 cm), and IV (150 cm) of the combustor. Previous work on this combustor showed that a pilot flame with an equivalence ratio less than that of the main flame resulted in a higher instability amplitude [27]. High-fidelity large-eddy simulation in the previous study suggested that the main flame loses heat to the relatively colder region of the pilot, weakening the stabilization of the flame near the centerbody and making it more susceptible to thermoacoustic oscillation. This same behavior is seen in the Type I conditions in this study. While increasing Π reduces the amplitude of the instability for Modes III and IV, it does not completely suppress the instability in either mode. Previous work showed that Mode IV cannot be suppressed using pilot flames at the Baseline condition, although it has been successful in suppressing Mode III [37].

Figure 11 shows the impact of piloting on the C17 condition, an example of the Type II conditions, for all combustor lengths. Modes I and III of the combustor are unstable at Π=0%, likely a result of the heat loss from the flame to the pilot region. Instability amplitude continually decreases in all modes with increasing Π. Figure 12 shows the impact of pilot on the N15 condition, an example of the Type III conditions. At Π=0%, the instability amplitude is similar to the Π=5% case for combustor lengths of 63.5-89 cm, but the instability is suppressed at lengths of 91 cm and above with a step change in amplitude.

This step change in instability amplitude is repeatable and is a result of flame liftoff from the ORZ. The low-pilot condition likely reduces the temperature near the attachment zone of the flame and causes extinction in the base region near the ORZ. For combustor lengths less than 94 cm, increasing Π decreases the amplitude of the instability. Further, the combustor length at which the flame is

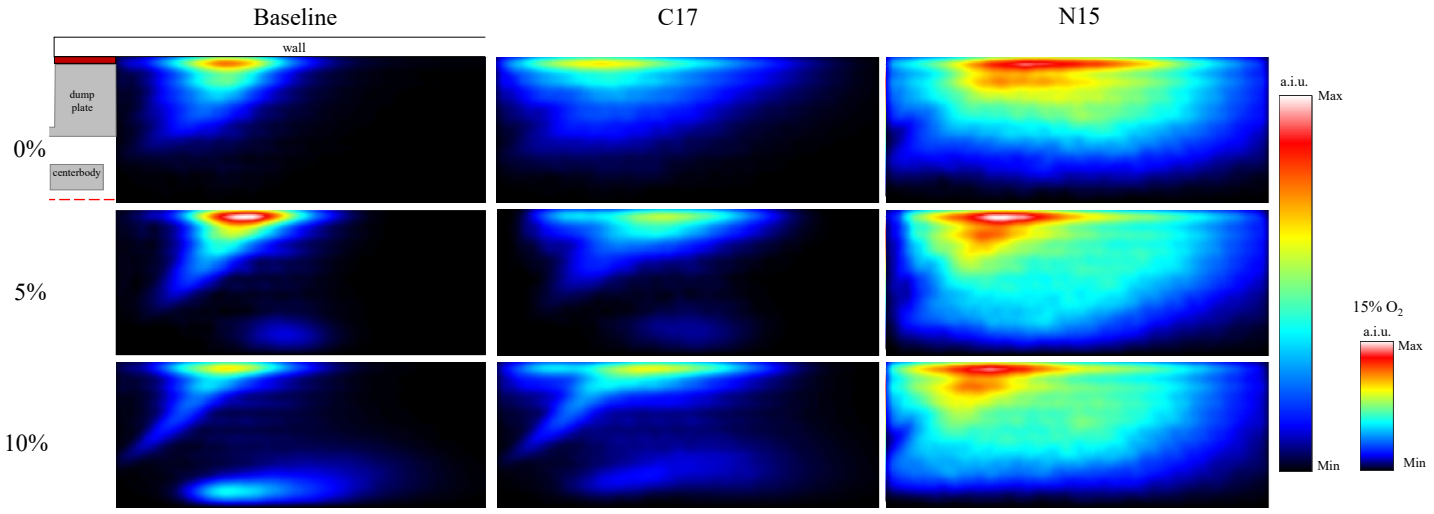

Figure 13. Abel-inverted, time-average flame structure with increasing pilot percentage for the three main types of behaviors at a combustor length of 63.5 cm.

stable decreases with increasing Π for Π > 0%. However, no level of Π is able to completely stabilize the flame at the shortest combustor lengths (63.5-76 cm).

The pilot also has an impact on the instability frequency in the Type III cases, whereas the pilot had no effect on instability frequency in Type I and II cases. In general, the instability frequency increases with increasing pilot for the Type III cases. We hypothesize that the frequency increase is driven by an increase in recirculation velocity in the central recirculation zone. Increasing Π results in more gas expansion in the central recirculation zone as the heat release from the pilot flame increases. More gas expansion could result in higher velocities in the recirculation region, and hence shorter timescales for recirculation and reignition. Also, higher temperatures in the central region of the combustor would aid the ignition of fresh reactants being injected, which would also shorten the timescale of each oscillation. LES results from Li et al. [27] shows an increase in recirculation strength and velocity with higher equivalence ratio in the pilot flame for a given pilot flow rate, which supports our hypothesis about the instability mechanism at low-oxygen conditions.

Figure 13 shows the impact of the pilot on the time-averaged structure of the flame for the three conditions shown in Figure 10-Figure 12. The figure shows examples of Type I (Baseline), II (C17), and III (N15) conditions with increasing Π from top to bottom; the color scale for the Type I and II cases are the same and the color scale for the Type III case has been altered to make the structure

clearer. As Π increases, the intensity of the pilot flame increases along the centerline in all cases, although the pilot jet is quite weak in the N15 case as compared to the other two. Given that the global equivalence ratio of the flame is kept constant as the pilot fuel is added, the intensity of the main flame decreases with increasing Π since the main-flame equivalence ratio decreases. Despite the decreasing main-flame equivalence ratio, the addition of pilot fuel increases the intensity of the flame near the anchoring point at the centerbody in all cases. For example, the C17 case has very little flame intensity near the bottom left of the image at Π=0%, which is where the centerbody is located. At Π=10%, the flame is stabilized on the centerbody. Previous simulations of this configuration suggest that this higher-intensity stabilization zone is a result of the back-support provided by the richer pilot flame [27]. Increase in the flame intensity signal near the centerbody is even present in the Type III case (N15), despite the very diffuse flame at this condition. Visual observation during experiments suggests that the flame never stabilizes on the centerbody like it does in the high-O_2 cases, but instead is better supported along the centerline by the addition of fuel to that region. Further, the addition of pilot encourages flame stabilization in the ORZ for the high-N_2 cases.

The addition of the pilot flame does not change the mechanism of flame oscillation in any of the cases, despite decreasing the oscillation amplitude. Figure 14 shows the Abel-inverted, phase-resolved fluctuation images of one oscillation cycle for the Type I (Baseline) and Type III (N15) conditions at 63.5 cm combustor length and Π=10% pilot. The images are normalized to the maximum intensity for each case. For the Baseline case, the high pilot suppresses the pressure oscillations. What little fluctuation occurs in the flame has the same convective pattern as in the cases with lower Π. In contrast, the N15 condition cannot be stabilized even with high pilot levels. The flame is unstable and exhibits strong fluctuations with no noticeable change in the instability mechanism. The instability for N15 still originates at the centerline and travels outwards towards the wall regions with noticeable activity in the ORZ.

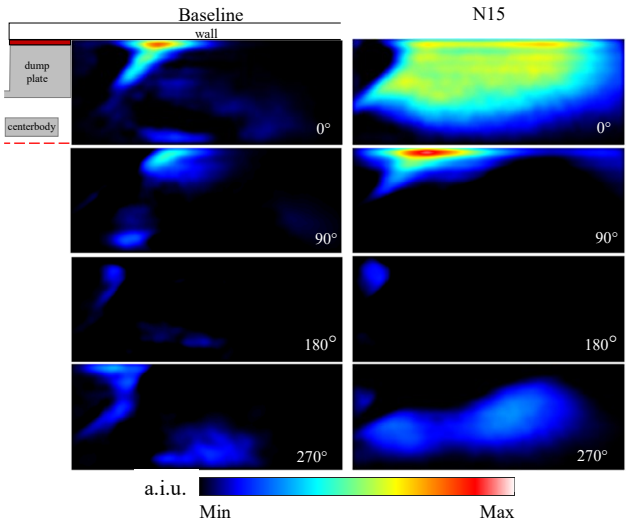

Figure 14. Abel-inverted, phase-resolved flame oscillation images for Type I and Type III behavior at 63.5 cm combustor length and Π=10%.

CONCLUSIONS

In this work, we considered the impact of different levels and compositions of diluents on the static and dynamic stability of a piloted swirl-stabilized flame. Three types of flame shapes and thermoacoustic oscillation behaviors were encountered. Type I conditions at high-O_2 content were strongly stabilized on the nozzle centerbody and exhibited typical thermoacoustic oscillations that moderately respond to piloting. Type II conditions had a weakly-anchored flame that had no thermoacoustic oscillations across all combustor lengths. Type III conditions exhibited a lifted, highly diffuse flame with low-frequency oscillations that had an ignition/extinction behavior rather than a convecting disturbance along the flame. These low-frequency oscillations were not replicated with open-loop forcing like the higher-frequency, velocity-coupled oscillations at the high-O_2 conditions were. Additionally, we showed that the low-frequency instabilities are dependent on the diluent composition at low-O_2 conditions. Compositions with higher levels of CO_2 were not repeatable and the flame was less anchored near the dump plane. Compositions with higher levels of N_2 showed stronger anchoring in the ORZ, which led to more repeatable instability behaviors. Finally, we showed that piloting can improve Type I and II conditions, both statically and dynamically. However, the levels of piloting tested here only showed moderate improvement in the dynamic stability of Type III conditions, with no improvement in static stability.

Several differences in the properties of each of these mixtures changed the shape and dynamics of the flame. In particular, changes in unstretched laminar flame speed, stretched flame speed, and extinction strain rate, correlated well with the observed changes in flame structure. At the lowest oxygen content mixtures (15% O_2), the composition of the diluent mixtures had a significant effect on the stretched flame behavior. The high-CO_2 mixtures had lower flame speeds and significantly lower extinction strain rates than the high-N_2 mixtures. These differences are likely the reason for differences in flame holding, particularly in the high-strain region of the ORZ.

The results of this study have several implications for the introduction of EGR in gas turbine engines. First, the addition of EGR has significant effects on both the static and dynamic stability of the flame at a given flame temperature. The changes to the static stability could affect the ability for turndown by changing the blowoff limits of the flame. Even at a given engine load, the significant changes to the flame shape could have implications for pattern factor and hence high-pressure turbine durability. The changes in the coupling mechanism of the combustion oscillation – from a velocity-coupled instability to an ignition/extinction-driven oscillation – could require changes to oscillation control strategies. Traditional oscillation control methods are developed to suppress thermoacoustic instabilities and may not be effective at suppressing instabilities driven by extinction behaviors.

The final important outcome of this work is the impact of diluent composition on the stability of the flame. At a given O_2 level, the flame displayed significantly different stability maps and oscillation patterns when the diluent composition was high in N_2 vs. CO_2. Further testing that was not presented in this paper suggests that the behavior is a result of sensitivity to CO_2 concentration at a given O_2 level. If this is the case, then increasing the level of CO_2 in a diluent mixture can have highly destabilizing effects despite the increase in efficiency of a CO_2 sequestration process with increased CO_2 concentration. Further investigation is necessary to understand the chemical pathways that may be responsible for the sensitivity to CO_2 concentration. Additionally, the stretched flame behavior of the diluted mixtures was shown to be different from that of the baseline condition. As such, matching flame temperature, as one would do for an engine operating at a constant firing temperature, does not guarantee the same propagation behavior or flame stability. In order to match flame stability across a range of EGR levels, a constant flame-speed operating mode will most likely be necessary, which would have implications for how engine operators run the engine.

ACKNOWLEDGEMENTS

The authors are grateful for the financial support from Solar Turbines Incorporated with program monitor Dave Voss.

REFERENCES

[1] Pörtner, H.-O., et al. (2022). "Technical Summary." Pörtner H.-O. et al. (eds.). In: *Climate Change 2022: Impacts, Adaptation and Vulnerability. Contribution of Working Group II to the Sixth Assessment Report of the Intergovernmental Panel on Climate Change*. Cambridge University Press, pp. 37–118.

[2] EPA (2022). "Inventory of U.S. Greenhouse Gas Emissions and Sinks: 1990-2020." U.S. Environmental Protection Agency, EPA 430-R-22-003. https://www.epa.gov/ghgemissions/inventory-us-greenhouse-gas-emissions-and-sinks-1990-2020.

[3] Administration U.S. Energy Information. (2022). "Monthly Energy Review August 2022," https://www.eia.gov/totalenergy/data/monthly/

[4] Songolzadeh, M., Soleimani, M., Takht Ravanchi, M., & Songolzadeh, R. (2014). "Carbon dioxide separation from flue gases: A technological review emphasizing reduction in greenhouse gas emissions," *The Scientific World Journal*, p. 828131.

[5] Zamarripa, M. A., Eslick, J. C., Matuszewski, M. S., & Miller, D. C. (2018). "Multi-objective optimization of membrane-based CO_2 capture" In: *13 International Symposium on Process Systems Engineering (PSE 2018)*, Vol. 44, pp. 1117–1122.

[6] Hasan, M. M. F., Baliban, R. C., Elia, J. A., & Floudas, C. A. (2012). “Modeling, simulation, and optimization of post-combustion CO_2 capture for variable feed concentration and flow rate. 1. Chemical absorption and membrane processes.” *Industrial & Engineering Chemistry Research*, Vol. 51, No. 48, p. 15642–15664.

[7] Drage, T. C., Snape, C. E., Stevens, L. A., Wood, J., Wang, J., Cooper, A. I., Dawson, R., & Guo, X. (2012). “Step Change Adsorbents and Processes for CO2 Capture.” In: *Advances in Gas Processing,* Vol. 3, pp. 30–37.

[8] Burnes, D., & Saxena, P. (2022). “Operational scenarios of a gas turbine using exhaust gas recirculation for carbon capture.” *Journal of Engineering for Gas Turbines and Power*, Vol. 144, No. 2, p. 1–12.

[9] Burnes, D, Saxena, P, & Dunn, P. (2020). “Study of using exhaust gas Recirculation on a gas turbine for carbon capture.” *ASME Turbo Expo,* Virtual, Online.

[10] ElKady, A. M., Evulet, A., Brand, A., Ursin, T. P., & Lynghjem, A. (2009). “Application of exhaust gas recirculation in a DLN F-class combustion system for post-combustion carbon capture.” *Journal of Engineering for Gas Turbines and Power*, Vol. 131, No. 3, p. 034505.

[11] Zaidaoui, H., Boushaki, T., Sautet, J. C., Chauveau, C., Sarh, B., & Gökalp, I. (2018). “Effects of CO_2 dilution and O2 enrichment on non-premixed turbulent CH_4-air flames in a swirl burner.” *Combustion Science and Technology*, Vol. 190, No. 5, p. 784–802.

[12] Roy, R., & Gupta, A. K. (2020). “Flame structure and emission signature in distributed combustion.” *Fuel*, Vol. 262, p. 116460.

[13] Shareh, F. B., Silcox, G., & Eddings, E. G. (2018). “Calculated impacts of diluents on flame temperature, ignition delay, and flame speed of methane-oxygen mixtures at high pressure and low to moderate temperatures.” *Energy and Fuels*, Vol. 32, No. 3, p. 3891–3899.

[14] De Santis, A., Ingham, D. B., Ma, L., & Pourkashanian, M. (2016). “CFD analysis of exhaust gas recirculation in a micro gas turbine combustor for CO_2 capture.” *Fuel*, Vol. 173, p. 146–154.

[15] Natarajan, J., Lieuwen, T., & Seitzman, J. (2007). “Laminar flame speeds of H_2/CO mixtures: Effect of CO_2 dilution, preheat temperature, and pressure.” *Combustion and Flame*, Vol. 151, No. 1, p. 104–119.

[16] Galmiche, B., Halter, F., Foucher, F., & Dagaut, P. (2011). “Effects of dilution on laminar burning velocity of premixed methane/air flames.” *Energy and Fuels*, Vol. 25, No. 3, p. 948–954.

[17] Ermel, J, Richter, S, Kick, T, Braun-Unkhoff, M, Naumann, C, & Riedel, U. (2015). "The Influence of Diluent Gases on Combustion Properties of Natural Gas: A Combined Experimental and Modeling Study." *ASME Turbo Expo*, Montreal, Quebec, Canada.

[18] Foley, C., Chterev, I., Noble, B., Seitzman, J., & Lieuwen, T. (2017). “Shear layer flame stabilization sensitivities in a swirling flow.” *International Journal of Spray and Combustion Dynamics*, Vol. 9. No. 1, p. 3–18.

[19] Watanabe, H., Shanbhogue, S. J., & Ghoniem, A. F. (2015). “Impact of equivalence ratio on the macrostructure of premixed swirling CH_4/Air and $CH_4/O_2/CO_2$ flames.” *ASME Turbo Expo,* Montreal, Quebec, Canada.

[20] Terhaar, S., Oberleithner, K., & Paschereit, C. O. (2014). "Impact of steam-dilution on the flame shape and coherent structures in swirl-stabilized combustors.” *Combustion Science and Technology*, Vol. 186, No. 7, p. 889–911.

[21] Goke, S., Terhaar, S., Schimek, S., Gockeler, K., & Paschereit, C.O. (2011) "Combustion of natural gas, hydrogen and bio-fuels at ultra-wet conditions." *ASME Turbo Expo,* Vancouver, British Columbia, Canada.

[22] Rizk, N. K., & Lefebvre, A. H. (1984). “Influence of laminar flame speed on the blowoff velocity of bluff-body-stabilized flames.” *AIAA Journal*, Vol. 22, No. 10, p. 1444–1447.

[23] Lieuwen, T., Torres , H., Johnson , C., & Zinn, B. T. (2000). “A mechanism of combustion instability in lean premixed gas turbine combustors.” *Journal of Engineering for Gas Turbines and Power*, Vol. 123, No. 1, p. 182–189.

[24] Ferguson, D, Ranalli, JA, & Strakey, P. (2010). "Influence of exhaust gas recirculation on combustion instabilities in CH_4 and H_2/CH_4 fuel mixtures." *ASME Turbo Expo,* Glasgow, UK.

[25] Evulet, A. T., ELKady, A. M., Branda, A. R., & Chinn, D. (2009). “On the performance and operability of GE’s dry low NOx combustors utilizing exhaust gas recirculation for post-combustion carbon capture.” *Energy Procedia*, Vol. 1, No. 1, p. 3809–3816.

[26] Li, J, Peluso, S, Quay, B, Santavicca, D, Blust, J, & Srinivasan, R. (2017). “Effect of pilot flame on flame macrostructure and combustion instability.” *ASME Turbo Expo,* Charlotte, North Carolina, USA.

[27] Li, J., Kwon, H., Seksinsky, D., Doleiden, D., O'Connor, J., Xuan, Y., Akiki, M., & Blust, J. (2021). “Describing the mechanism of instability suppression using a central pilot flame with coupled experiments and simulations.” *Journal of Engineering for Gas Turbines and Power,* Vol. 144, No. 1, p. 011015.

[28] Albrecht, P., Bade, S., Lacarelle, A., Paschereit, C. O., & Gutmark, E. (2010). “Instability control by premixed pilot flames.” *Journal of Engineering for Gas Turbines and Power,* Vol. 132, No. 4, p. 041501.

[29] Albrecht, P., Speck, S., Schimek, S., Bauermeister, F., Gutmark, E., & Paschereit, O. (2007). “Lean blowout control using an auxiliary premixed flame in a swirl-stabilized combustor.” *43rd AIAA/ASME/SAE/ASEE Joint Propulsion Conference & Exhibit*. Cincinnati, OH, USA.

[30] Waser, M. P. (1984) “Introduction to the two-microphone cross-spectral method of determining sound intensity,” *Noise Control Engineering Journal,* Vol. 2, No. 3, p. 76–85.

[31] Smith, G.P., Golden, D.M., Frenklach, M., Moriarty, M.W., Eiteneer, B., Goldenberg, M., Bowman, C.T., Hanson, R.K., Song, S., Gardiner, Jr., W.C., Lissianski, V.V., & Qin, Z. “GRIMech 3.0,” http://www.me.berkeley.edu/gri_mech/

[32] Alvarez, R., Rodero, A. & Quintero, M.C. (2002). “An Abel inversion method for radially resolved measurements in the axial injection torch”. *Spectrochimica Acta Part B: Atomic Spectroscopy*, Vol. 57, No. 11, p. 1665-1680.

[33] R.J. Kee, F.M. Rupley, J.A. Miller, M.E. Coltrin, J.F. Grcar, E. Meeks, H.K. Moffat, A.E. Lutz, G. Dixon-Lewis, M.D. Smooke, J. Warnatz, G.H. Evans, R.S. Larson, R.E. Mitchell, L.R. Petzold, W.C. Reynolds, M. Caracotsions, W.E. Stewart, P. Glarborg, C. Wang, O. Adigun, Ansys Chemkin-Pro 2022 R1, (2022).

[34] Li, J, Peluso, S, Santavicca, D, & Blust, J. (2019). "Effect of a premixed pilot flame on the velocity-forced flame response in a lean-premixed swirl-stabilized combustor." *ASME Turbo Expo,* Phoenix, Arizona, USA.

[35] Zhang, Q., Shanbhogue, S.J., Shreekrishna, Lieuwen, T. and O'Connor, J. (2011). “Strain characteristics near the flame attachment point in a swirling flow.” *Combustion Science and Technology*, Vol. 183, No. 7, p. 665-685.

[36] Shanbhogue, S.J., Sanusi, Y.S., Taamallah, S., Habib, M.A., Mokheimer, E.M.A. and Ghoniem, A.F. (2016). “Flame macrostructures, combustion instability and extinction strain scaling in swirl-stabilized premixed CH4/H2 combustion.” *Combustion and Flame*, Vol. 163, p. 494-507.

[37] Doleiden, D. (2022) “Understanding the limits of combustion instability suppression mechanisms,” Ph.D. Thesis, The Pennsylvania State University.

[38] O’Meara, B. (2015) “An experimental study of the effect of a pilot flame on technically pre-mixed, self-excited combustion instabilities,” Ph.D. Thesis, The Pennsylvania State University.

[39] Doleiden, D, Karmarkar, A, O’Connor, J, & Blust, J. (2022). "Impact of central piloting on the static and dynamic stability of swirl-stabilized flames." *ASME Turbo Expo,* Rotterdam, The Netherlands.